Remote Sens. **2015**, *7*, 11954-11973; doi:10.3390/rs70911954

OPEN ACCESS

remote sensing

ISSN 2072-4292

www.mdpi.com/journal/remotesensing

Article

Rapid Response to a Typhoon-Induced Flood with an SAR-Derived Map of Inundated Areas: Case Study and Validation

Hsiao-Wei Chung [1], Cheng-Chien Liu [1,2,*], I-Fan Cheng [2], Yun-Ruei Lee [2] and Ming-Chang Shieh [3]

[1] Department of Earth Sciences, National Cheng Kung University, No. 1, Ta-Hsueh Road, Tainan 701, Taiwan; E-Mail: l48001032@mail.ncku.edu.tw

[2] Global Earth Observation and Data Analysis Center, National Cheng Kung University, No. 1, Ta-Hsueh Road, Tainan 701, Taiwan; E-Mails: t741213@yahoo.com.tw (I.-F.C.); beaduck@hotmail.com.tw (Y.-R.L.)

[3] Water Hazard Mitigation Center, Water Resources Agency, 9-12F., No. 41-3, Sec. 3, Xinyi Rd., Da'an Dist., Taipei 106, Taiwan; E-Mail: A680010@ms1.wra.gov.tw

* Author to whom correspondence should be addressed; E-Mail: ccliu88@mail.ncku.edu.tw; Tel.: +886-6-2757575 (ext. 65422); Fax: +886-6-2740285.

Academic Editors: Guy J-P. Schumann, Zhong Lu and Prasad S. Thenkabail

Received: 30 June 2015 / Accepted: 3 September 2015 / Published: 18 September 2015

Abstract: We report the successful case of a rapid response to a flash flood in I-Lan County of Taiwan with a map of inundated areas derived from COSMO-SkyMed 1 radar satellite imagery within 24 hours. The flood was caused by the intensive precipitation brought by Typhoon Soulik in July 2013. Based on the ensemble forecasts of trajectory, an urgent request of spaceborne SAR imagery was made 24 hours before Typhoon Soulik made landfall. Two COSMO-SkyMed images were successfully acquired when the center of Typhoon Soulik had just crossed the northern part of Taiwan. The standard level-1b product (radiometric-corrected, geometric-calibrated and orthorectified image) was generated by using the off-the-shelf SARscape software. Following the same approach used with the Expert Landslide and Shadow Area Delineating System, the regional threshold of each tile image was determined to delineate still water surface and quasi-inundated areas in a fully-automatic manner. The results were overlaid on a digital elevation model, and the same tile was visually compared to an optical image taken by Formosat-2 before this event. With this ancillary information, the inundated areas were accurately and quickly identified. The SAR-derived map of inundated areas was

published on a web-based platform powered by Google Earth within 24 hours, with the aim of supporting the decision-making process of disaster prevention and mitigation. A detailed validation was made afterwards by comparing the map with *in situ* data of the water levels at 17 stations. The results demonstrate the feasibility of rapidly responding to a typhoon-induced flood with a spaceborne SAR-derived map of inundated areas. A standard operating procedure was derived from this work and followed by the Water Hazard Mitigation Center of the Water Resources Agency, Taiwan, in subsequent typhoon seasons, such as Typhoon Trami (August, 2013) and Typhoon Soudelor (August, 2015).

Keywords: remote sensing; synthetic aperture radar imagery; visible imagery; flooding; flood hazard mapping

1. Introduction

The effects of climate change are causing an increase in the frequency of environmental disasters around the world [1]. Among these, floods not only lead to significant economic losses, but also pose a threat to human life [2]. This issue is especially important in Taiwan, which has an annual typhoon season and geographic features that make certain areas prone to flooding. Moreover, both social and economic developments in Taiwan bring significant changes of land use inevitably, and these will also affect the frequency of flooding disasters in highland and urban areas. Recent assessments of a few major disasters reveal that collecting and interpreting remote sensing data not only provides critical information for emergency response support and relative decision making; the comprehensive analysis, integration and application of these data also offer great help for evacuation warning, disaster mitigation and rescue of victims [3,4]. Therefore, Taiwan's government has been endeavoring to acquire remote sensing imagery and to derive a map of inundated areas to manage and mitigate the catastrophic disaster caused by floods.

Among various remote sensing data, optical imagery with high spatial resolution and large coverage is widely used for deriving flood extent [5] by applying the multispectral signals to classify the moisture content of soil [6,7]. For example, Zhang *et al.* [8] blended the MODIS and Landsat images for urban flood mapping. A similar task was accomplished by Feng *et al.* [9] with some high spatial resolution imagery taken from an unmanned aerial vehicle. Jung *et al.* [10] used Landsat-5 Thematic Mapper images and the digital elevation model (DEM) to extract flood extent. Although a quite accurate map of inundated area can be derived from the optical imagery, it is not possible to obtain any real-time information of flood during the storm or typhoon [11], for the optical signals originated from the reflected sunlight would be covered by clouds. By contrast, the capability of acquiring imagery at all weather conditions makes the spaceborne radar imagery an ideal source of remote sensing data to derive the map of inundated areas for emergency response and relative decision making during the storm or typhoon.

Since SeaSAT-1's launch in 1978, more than 15 different spaceborne synthetic aperture radars (SAR) have been operated in orbit with wavelengths for microwave ranging from L-band (15–30 cm), S-band (7.5–15 cm), C-band (3.75–7.5 cm) to X-band (2.5–3.5 cm). SAR imagery has played an ever-increasing role in flood disaster assessment [12,13], geological survey [14], marine oil spills [15],

crops [16] and ecological assessment [17]. As early as 1987, spaceborne SAR imagery has been used to attempt to delineate the boundary of flooded areas [18,19]. Mason *et al.* [20] showed near real-time flood detection in urban and rural areas based on high resolution SAR images. Kundu *et al.* [21] applied a serial of RADARSAT-1 images to monitor the flood duration and extent, as well as the depth in Odisha, India. Their results were validated by field survey photos and information from local people. Manjusree *et al.* [22] used the optical data to validate an inundation map that was derived from SAR data. The optical imagery, however, provides no information if the study area is covered by clouds. To support crisis management and rescue activities with near real-time flood information during the flood event, it is therefore necessary to rapidly process the spaceborne SAR imagery and to deliver the inundation map to the end users [23,24]. From the operational point of view, three main challenges are: (1) how fast can the map be derived; (2) what is the accuracy of the map; and (3) can the flood depth be inferred, as well?

This research attempts to answer those three questions by reporting a case of rapidly responding to a flash flood in I-Lan County of Taiwan with a map of inundated areas derived from COSMO-SkyMed 1 radar satellite imagery within 24 hours. This work demonstrates the feasibility of rapidly responding to a typhoon-induced flood with a spaceborne SAR-derived map of inundated areas. A standard operating procedure was derived from this work and followed by the Water Hazard Mitigation Center (WHMC) of Water Resources Agency (WRA), Taiwan, in subsequent typhoon seasons, such as Typhoon Trami (August, 2013) and Typhoon Soudelor (August, 2015).

2. Flash Flood and Study Area

2.1. Typhoon Soulik

Typhoon Soulik developed as a mature tropical cyclone in the northern part of Guam on 8 July 2013, and its moving tracks forecasted at 20:00, 11 July, are shown in Figure 1. It brought strong winds and torrential rain and also caused floods, road collapses, rail and air traffic disruption and damage to electricity and communication systems. As a result, two people were killed; one person went missing; 123 people were injured; and the agricultural losses amounted to about 8.3 million U.S. dollars [25]. Since the sea alert was issued by the Central Weather Bureau (CWB) of Taiwan, a flood warning for I-Lan County was soon issued by WRA, which was therefore selected as our study area.

2.2. I-Lan County

I-Lan County, as shown in Figure 2, is located on the windward side of the northeast monsoon and receives the most rainfall among the other counties in Taiwan. The steep rivers and short currents of this region tend to rapidly centralize the rainfall downstream, thus causing floods. In particular, in the east part of the Lanyang Plain, the elevation is less than four meters, or even under the storm surge level, which makes it vulnerable to flooding. The geographical features also mean that orographic rains often occur in the Lanyang Plain, as it is surrounded by mountains on three sides, with a gap on the east coast. In winter, the northeast monsoon comes from this gap on the east side of I-Lan, and the rain that it brings can last for several months.

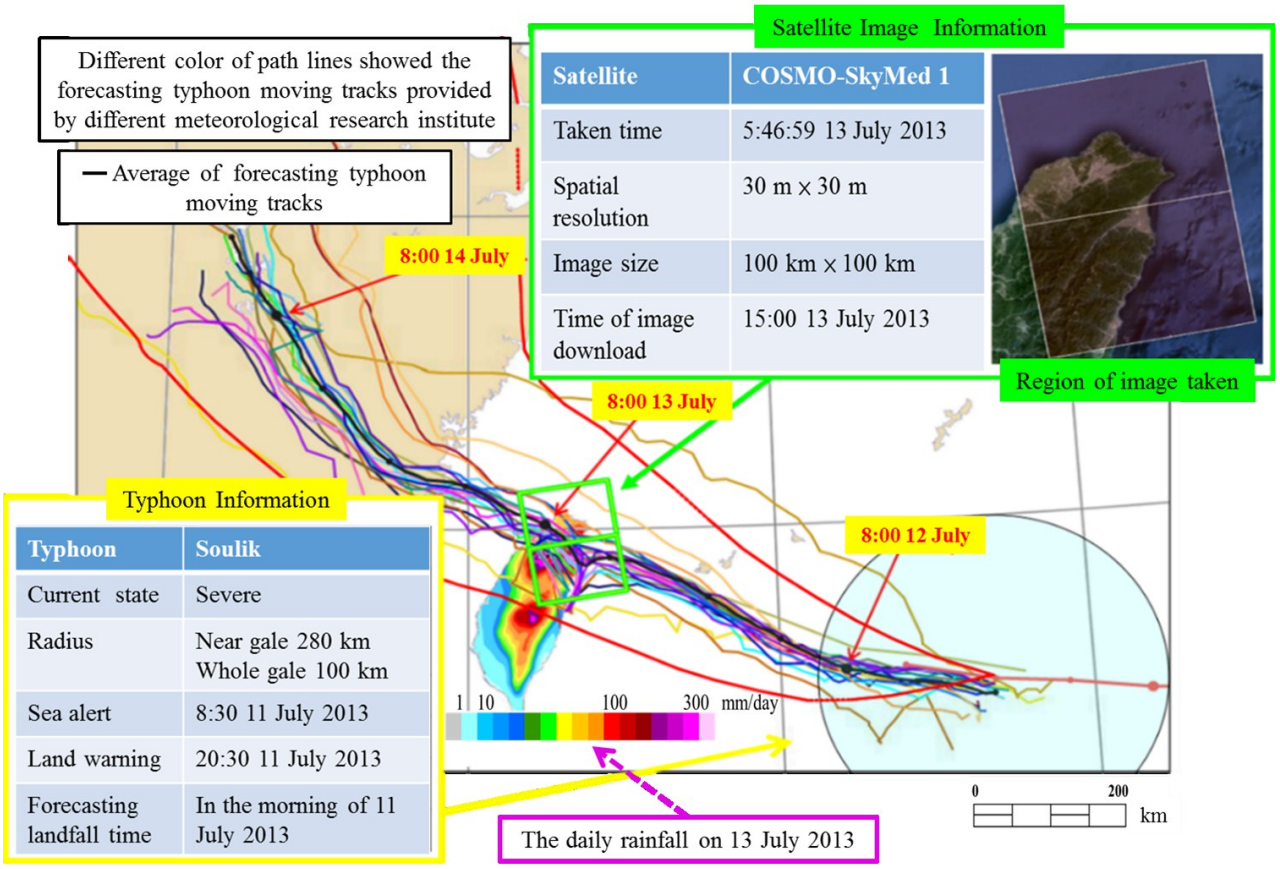

Figure 1. Information about Typhoon Soulik and its moving tracks forecasted at 20:00, 11 July. Two COSMO-SkyMed 1 radar satellite images with a spatial resolution of 30 m and a 100 × 100 km^2 coverage area were scheduled at 5:46:59, 13 July [26]. The region of the image taken is shown by the green box. The different colors of the path lines show the forecasted typhoon moving tracks provided by different forecasting models, such as the Weather Research and Forecasting Model (WRF) and the Fifth-Generation Penn State/ National Center for Atmospheric Research (NCAR) Mesoscale Model (MM5).

3. Data

3.1. SAR Image Request

When the sea alert for Typhoon Soulik was issued, we began to collect the typhoon path and rainfall forecast data provided by Taiwan Typhoon and Flood Research Institute (TTFRI) and CWB of Taiwan. The National Science and Technology Center for Disaster Reduction (NCDR) and WRA also decided to place an urgent order of radar satellite images of the I-Lan area before the land warning of Typhoon Soulik was issued. Two COSMO-SkyMed 1 radar satellite images with a spatial resolution of 30 m and a 100 × 100 km^2 coverage area were obtained during Typhoon Soulik, as shown in Figure 2b.

These images were taken at 05:47 on 13 July 2013, three hours after the typhoon's landfall, when Taiwan was still in the range of Soulik. The images were ready to be downloaded at 15:00. It took two hours to orthorectify the image, three hours to derive the flood region and two more hours to complete the flood and disaster damage estimations. Overall, the whole processing procedure was finished within 12 hours after acquiring the images, as shown in Table 1.

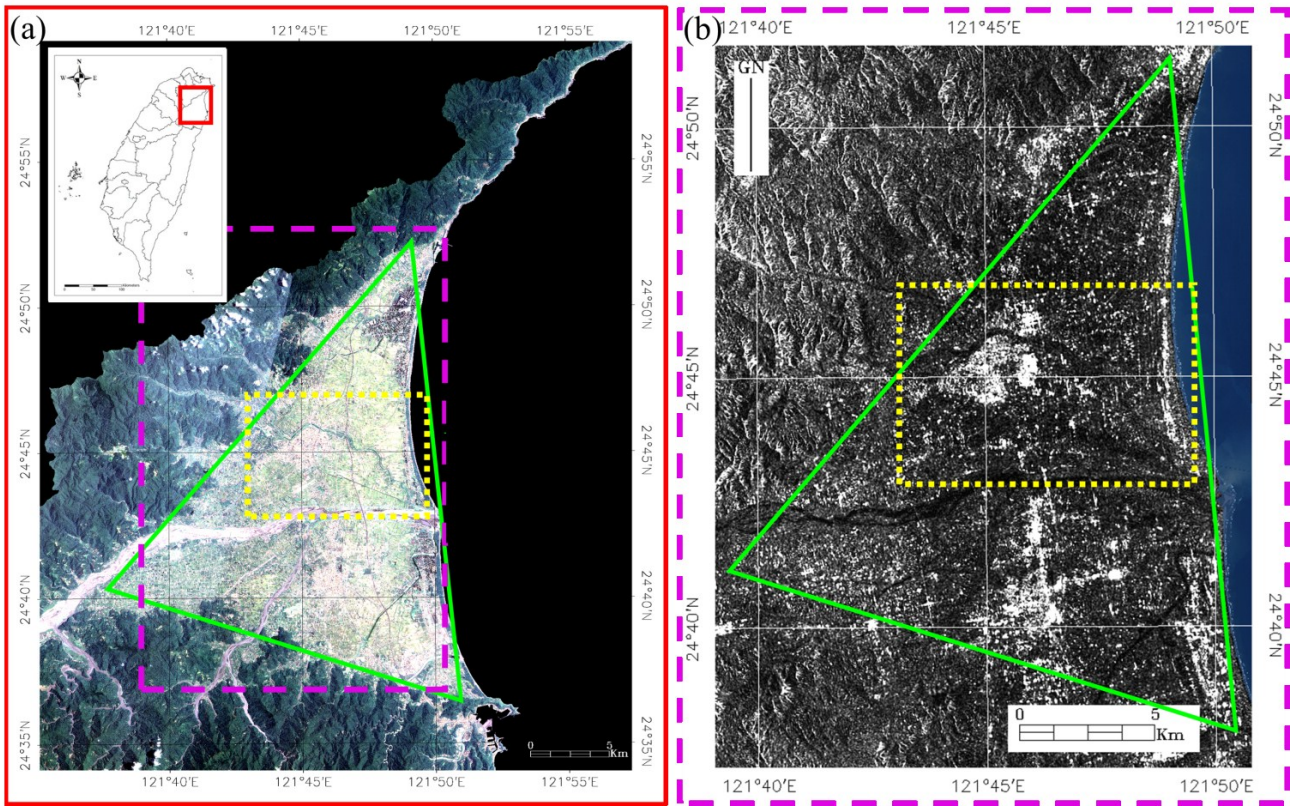

Figure 2. (**a**) Formosat-2 true color satellite image of I-Lan County, which is located in the northwestern part of Taiwan. The region in the green triangle is Lanyang Plain. (**b**) The region denoted as the purple square is covered by the SAR image. The region denoted as the yellow square is the same geographic position as the areas shown in Figure 3.

Table 1. The timetable of SAR image requesting, downloading and processing.

Steps	Time (Local Time in Taiwan)
Assessment of acquired image	8:30 a.m. 11 July 2013 (after a sea alert for the typhoon)
Place an urgent order	9:00 p.m. 11 July 2013 (after a land warning for typhoon)
Acquired SAR image	5:47 a.m. 13 July 2013 (three hours after making landfall)
SAR image download	3:00 p.m. 13 July 2013 (begin to download the image)
Image processing with SARscape	6:00 p.m. 13 July 2013 (two hours after downloading the image)
Derive the flood region	8:00 p.m. 13 July 2013 (five hours after downloading the image)

3.2. Synthetic Aperture Radar Imagery

Based on the sending and receiving delay, as well as the intensity and polarization signals of electromagnetic microwaves, radar satellites can penetrate the clouds and dust and detect variations of the land surface for all weather day and night [27,28]. A radar satellite platform can quickly and steadily move the entity radar antenna along the direction of its flight, and the accumulation of a series of restructured echo signals can last as long as several kilometers, acting like the antenna effect of a SAR. This overcomes the limitations of the radar beam width, and the antenna size is inversely proportional to the entity, thus dramatically improving the resolution of the azimuth. The Italian radar satellite, COSMO-SkyMed, has the world's shortest cycle revisit time, of about twelve hours. Taking three other

commercial satellites (TerraSAR-X, RADARSAT-1 and -2) into consideration, the revisit time interval can be further reduced to about eight hours.

After obtaining the SAR image, the ENVI SARscape commercial software was employed to make the geometric correction and radiometric correction. The enhanced Lee filter was then applied to remove speckle noise. Following the same approach as that applied in the Expert Landslide and Shadow Area Delineating System [29], the regional threshold of each tile image was determined to delineate still water surfaces and quasi-inundated areas in a fully-automatic manner, as explained in detail in Section 4.1.

3.3. Water Level Station

Both hydrologic and geographic factors are complicated in Taiwan, with high intensity rainfall and steep river slopes making the water levels of rivers change dramatically within a short time. It is thus necessary to obtain real-time hydrological measurement data to carry out rapid and effective floor control decisions. TTFRI has thus built water level stations in the I-Lan River, and the resulting *in situ* data of river water levels can be transmitted instantly. The positions of the water level stations are shown in Figure 3.

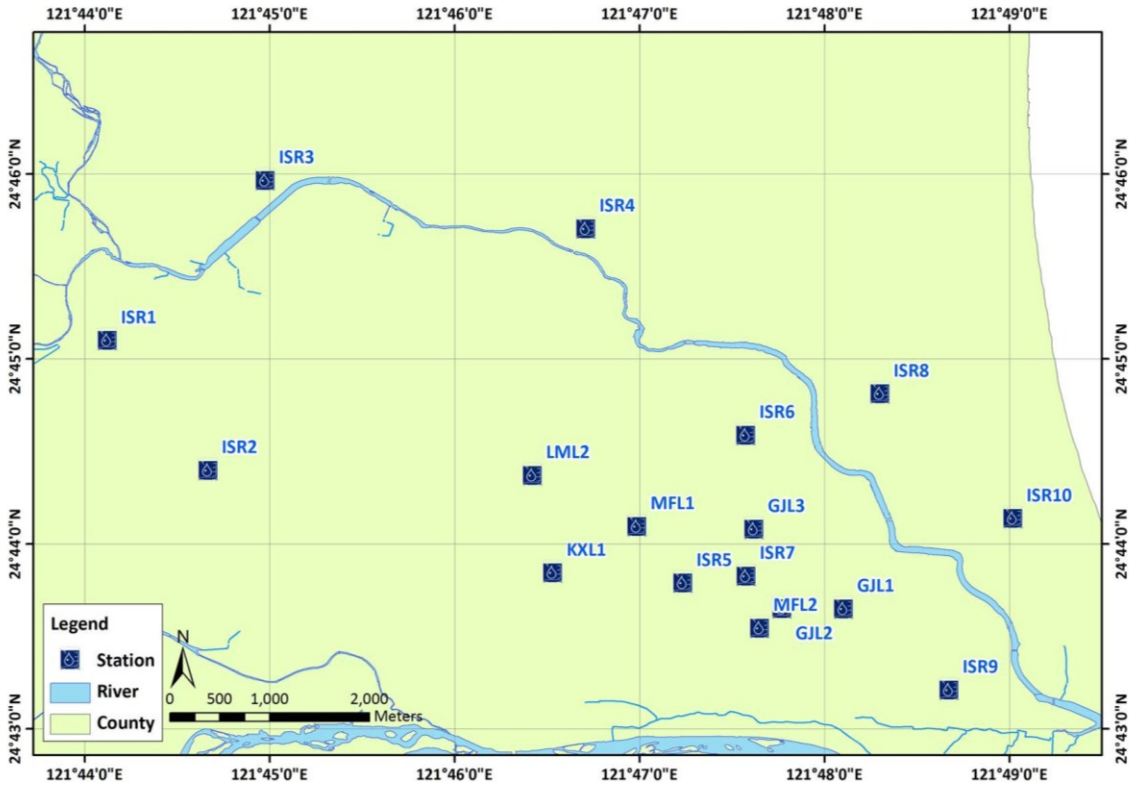

Figure 3. The positions of water level stations in the study area, with the geographic position being the same as that indicated by the yellow square in Figure 2.

4. Methods

4.1. Expert Synthetic Aperture Radar Imagery Waterbody Delineation System

Radar echo signals are mainly affected by terrain factors, such as dielectric constant (including moisture content), surface roughness and terrain slope. Wide and still water surfaces generally reflect any incident energy away from the radar, which then produces a black area that is easy to distinguish in radar images.

Since radar satellite signals can penetrate clouds and dust all day long, these have great practical value in tasks, such as aiding emergency responses during flood disasters. Martinis reviewed [30] the application of spaceborne SAR data for the rapid detection of flood regions, and he divided them into two categories: artificial and automatic interpretation.

The main errors of applying SAR images in detecting flood regions usually occur when: (1) the smooth surfaces of airport runways or highways that produce reflections are mistaken for actual inundated areas; (2) some dynamic water factors, such as wind-induced surface ripples, tend to increase water backscatter and reduce its surface contrast strength compared to other surface features; (3) vegetation that is not completely inundated might be highlighted as scattering signals that are then reflected again, and these highlighted spots should also be delineated as inundated areas; and (4) the perpendicular angles between buildings in urban areas and their surfaces may cause corner reflections, double reflections or even triple reflections, resulting in extremely bright spots on images. Meanwhile, high buildings would generate shadowing effects that cause a lot of dark areas without radar echo signals.

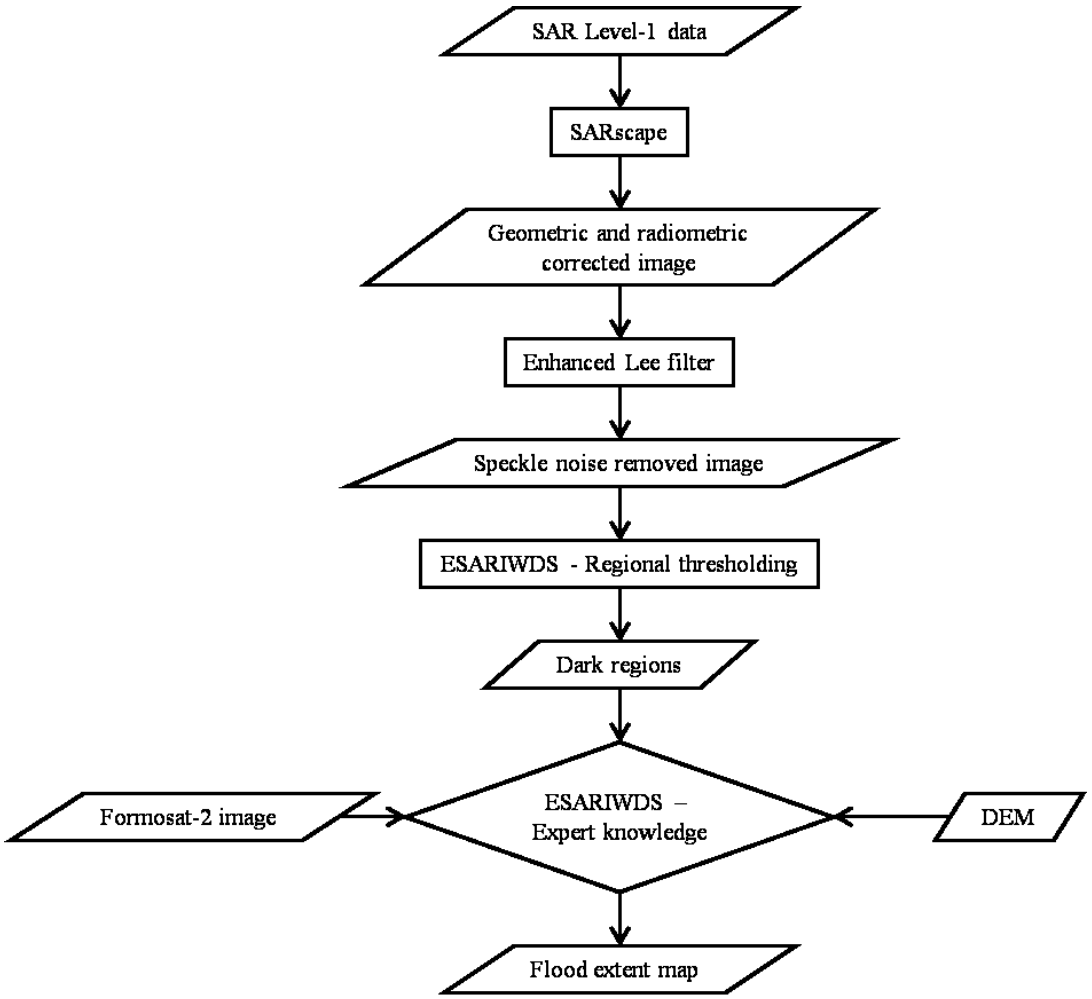

Figure 4. The flowchart of flood extent detection using the Expert Synthetic Aperture Radar Imagery Waterbody Delineation System (ESARIWDS).

To reduce the possible errors and to help the interpreters determine the flooded areas quickly and accurately, we developed the Expert Synthetic Aperture Radar Imagery Waterbody Delineation System (ESARIWDS) to detect the flood extent, following the approach described in [29]. Since it

is not easy to apply a universal threshold value to separate the flooded regions from the background in the entire SAR image, ESARIWDS divides the whole image into many scenes and calculates a regional threshold value of dark regions for each individual scene by searching the inflection point of histogram. Figure 4 gives the flowchart of the flood extent detection using ESARIWDS. For the case of a low ratio of a dark region in one scene, as shown in Figure 5a, the histogram exhibits a pattern of single peak (Figure 5b). The inflection point between 0 and the peak value gives an ideal threshold to accurately separate the dark regions from the background, as illustrated by the green polygons in Figure 5a. For the case of high ratio of the dark region in one scene, as shown in Figure 6a, the histogram exhibits a bimodal pattern (Figure 6b). The inflection point between the peak value and the valley gives an ideal threshold to accurately separate the dark regions from the background, as illustrated by the green polygons in Figure 6a.

So far, we have derived the dark regions from the SAR imagery. Because some smooth surfaces, such as airport runways or highways, would produce reflections that might be mistaken for the actual inundated areas, to effectively exclude these areas to get the flooded areas, we have to resort to other geospatial information. Considering the fact that the occurrence of flooded areas is usually related to topography, the most useful information in preparing a flood extent map is DEM. ESARIWDS enables users to overlay the SAR image and the boundaries of dark regions onto the corresponding DEM on-the-fly, as shown in Figure 7. Furthermore, the users can freely rotate and rescale the DEM in a 3D fashion. This provides the most intuitive way to examine the dark regions according to their adjacent changes in topography. To facilitate the interpretation, ESARIWDS also enables us to switch between the current SAR image and the optical image, such as the most recent Formosat-2 image. Note that the information is not meant to delineate the boundary of flood extent, but rather is used as supporting material to distinguish the inundated areas from the dark regions. Switching between the SAR image and the Formosat-2 optical image provides a convenient and unambiguous way to determine the inundated areas in a quick and accurate fashion.

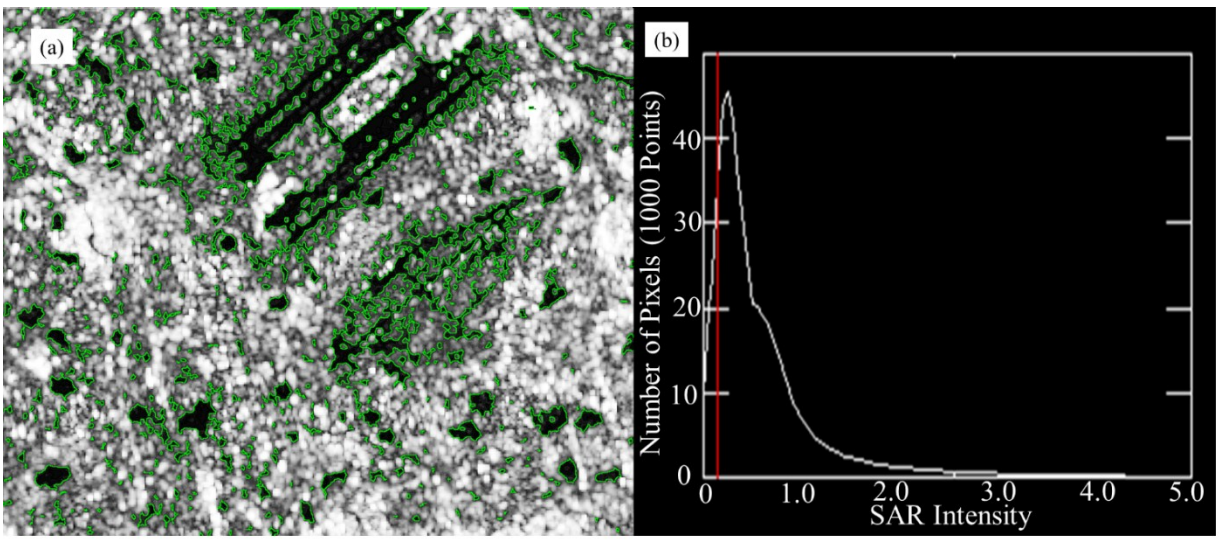

Figure 5. An example of the low ratio of the dark region in one scene. (**a**) Dark regions determined by ESARIWDS (green polygons). (**b**) Histogram of the current scene, which exhibits a pattern of a single peak.

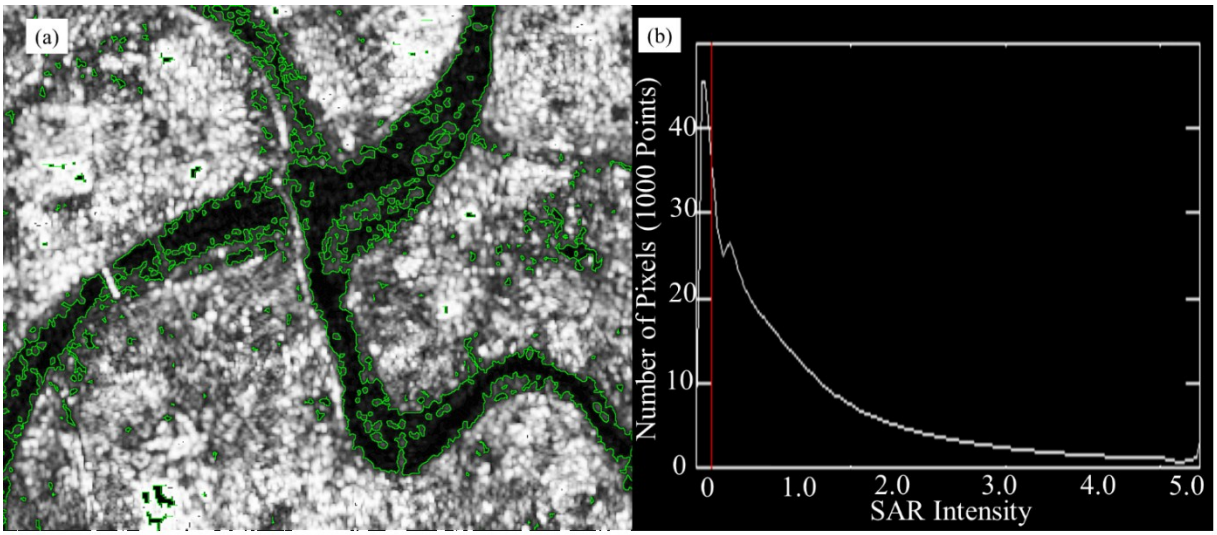

Figure 6. An example of the high ratio of the dark region in one scene. (**a**) Dark regions determined by ESARIWDS (green polygons). (**b**) Histogram of the current scene, which exhibits a bimodal pattern.

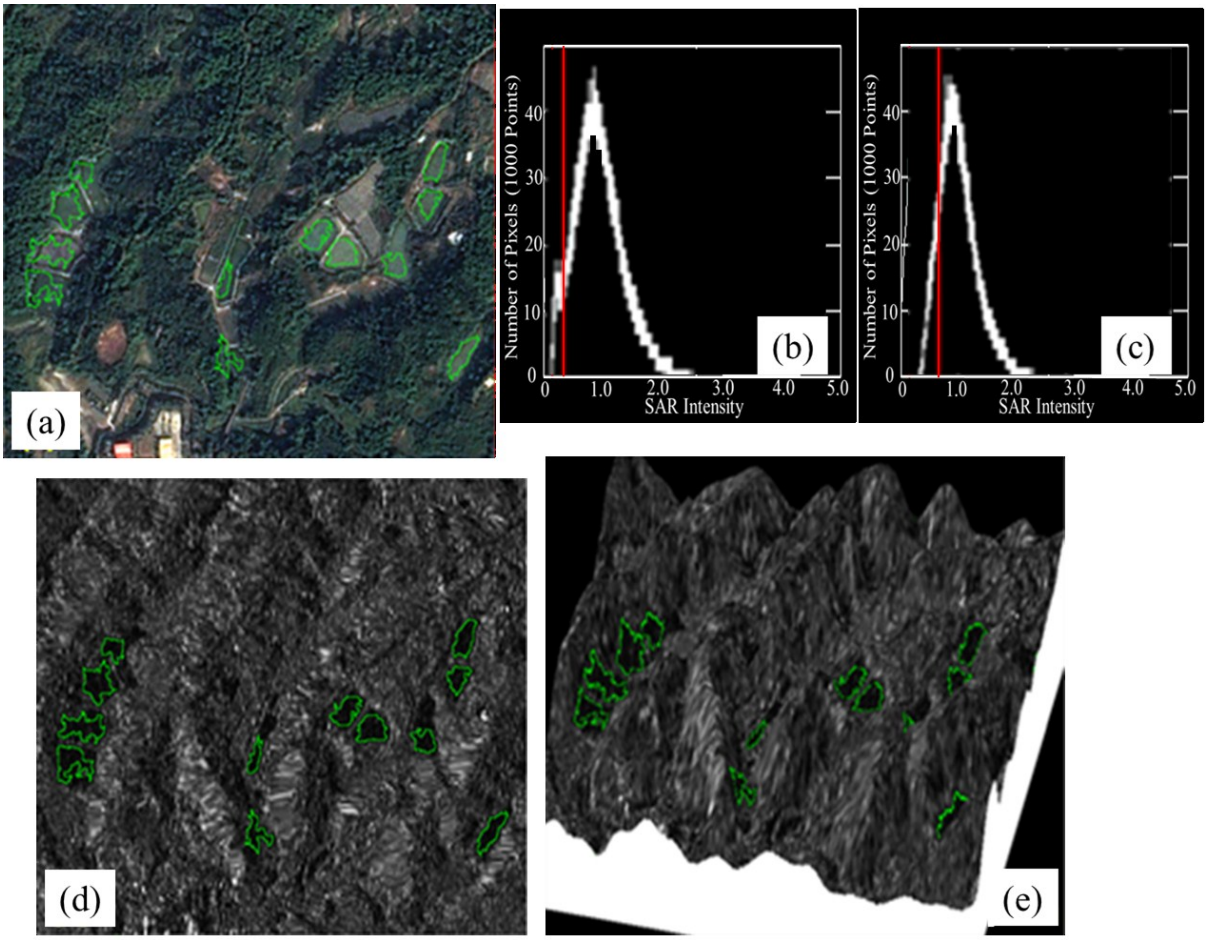

Figure 7. An example of flood extent detection using ESARIWDS. (**a**) The most recent optical image of the same area taken by Formosat-2; (**b**) like-polarization histogram; (**c**) cross-polarization histogram; (**d**) dark regions in the SAR image; (**e**) overlaying the SAR image and the boundary of dark regions onto the corresponding DEM to visually examine the topographical relationship of each dark region.

4.2. Flood Depth Deriving

Radar satellite signals can penetrate clouds and dust all day long, which makes them ideal for acquiring images at critical moments, especially when disasters occur. The actual depth that a radar signal can penetrate through the water itself, however, is very limited. It is therefore necessary to seek for an indirect way to infer the flood depth from the existing data we have. This research proposes to combine flooding patterns with the inundation potential maps produced by WRA from 2007 to 2010 to infer the flood depths.

The flooding simulation models that are often used include a one-dimensional quantity inundation model, a variable inundation model, a two-dimensional inundation model (or nuclear cell model) and a two-dimensional inundation model (including urban drainage flooding patterns, the SOBEK® [31] hydrodynamic model and FLO-2D® hydrodynamic model [32]). Each model has its own theoretical background and assumptions and, therefore, is applicable on different occasions. However, no matter what kind of inundation model is applied, the results must be calibrated and validated. After the inundation model has calculated the results of torrential rains or certain flooding events, these data should be calibrated and validated with the *in situ* data, such as flooding depth, range and duration. Based on this calibration, the parameters, such as assumptions, topography and structures, will be more appropriate with regard to the actual flood.

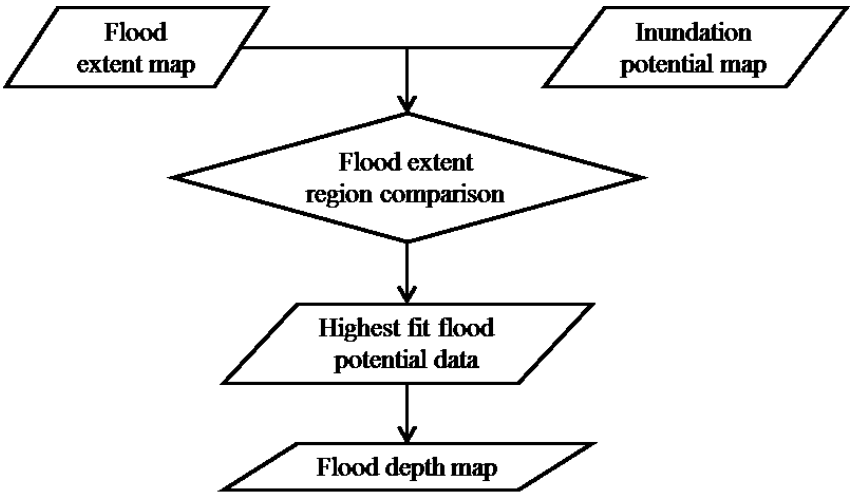

Figure 8. The flowchart of inferring the flood depths by combining flooding patterns with the inundation potential maps produced by WRA from 2007 to 2010.

Because past investigations of flood events were carried out with insufficient manpower, the records of actual flood observations are very inadequate. Therefore, the results of most simulation analyses of flooding events cannot be validated due to the lack of actual records that could be used as a reference. The SAR images that are taken during flood events can thus provide a more precise range of inundated areas and can be used as the validation data for the inundation simulation model. The steps used to infer the flood depths in this research are presented in the flow chart shown in Figure 8. The flood regions derived from the SAR image were compared to the inundation potential maps produced by the WRA from 2007 to 2010. The WRA built inundation potential maps for each city and county in Taiwan based on the draft of a handbook outlining the inundation potential map process and the related tests. The inundation potential map shows different recurrence periods based on different time intervals (1, 2, 5,

10, 15, 20, 25, 50, 100, 200 and 500 years) and different rainfall intensities (200, 350, 450 and 600 mm in one day). The relationship between flood region and inundation potential maps can be used to estimate the water depths at the time the image was taken.

The first step to obtaining the flood depth is collecting hourly precipitation data and the related hydraulic information and entering these into the inundation model. The model can then derive the flood potential map with both flood depth and region for each hour of the specific event. When combined with the flood regions that are calculated from the near real-time radar satellite images, the model can then start deriving the flood depths.

5. Results and Discussion

5.1. Inundation Extent

Typhoon Soulik developed as a mature tropical cyclone in the northern part of Guam on 8 July 2013. It brought strong winds and torrential rain, but also caused floods, road collapses, rail and air traffic disruption and electricity and communication systems damage. Once the sea alert for Typhoon Soulik was issued, we began to collect the typhoon path and rainfall forecast data provided by TTFRI and CWB of Taiwan. NCDR and WRA decided to take radar satellite images of the I-Lan area before the land typhoon alert for Soulik was issued. Two COSMO-SkyMed 1 radar satellite images were obtained during Typhoon Soulik. These images were taken at 05:47 on 13 July 2013, three hours after the typhoon's landfall, when Taiwan was still in the range of Soulik. The images were ready to be downloaded at 15:00. It took two hours to complete the process of orthorectification, three more hours to derive the flood regions and two more hours to complete the flood and disaster damage estimations. The whole processing procedure was finished within 12 hours after acquiring the images. Proud *et al.* [33] used Meteosat Second Generation (MSG) satellites to generate the rapid response flood map; this method was limited not only by cloud coverage, but also spatial resolution. Amarnath [34] also provided an algorithm: the Normalized Difference Surface Water Index for rapid flood inundation mapping; but, this algorithm depended on optical data, which are not suitable in rapid response to a typhoon-induced flood.

TTFRI provided *in situ* data of water levels with an interval of every ten minutes at 17 stations along the I-Lan River (as denoted in Figure 3). Figure 9 shows twelve stations that were fully in accordance with the interpretation results, while the other five stations with inconsistent results are shown in Figure 10. Note that the close-up photo of the water level gauge illustrates how the instrument is installed at each station. The inundated areas (red shaded polygons) interpreted from SAR imagery are overlaid on the optical images provided by Google Earth to indicate whether the station is flooded or not. It is also convenient to examine whether the station is located in a mixed pixel near the boundary of the inundated area. Because the spatial resolution of SAR imagery for this work is 30 m, quite a large zone around the boundary of the inundated area would be mixed pixels with signals from both land and water. If the station happens to be located in a mixed pixel, its signal would be biased by the mixed effect. After examining the location of each station and the boundary of inundated regions, we found that the GJL1, GJL3, KXL1, ISR2 and ISR5 stations are all located in mixed pixels, and they all give inconsistent results, as shown in Figure 10. If these five stations are eliminated from the analysis, the remaining twelve stations were fully in accordance with the interpretation results.

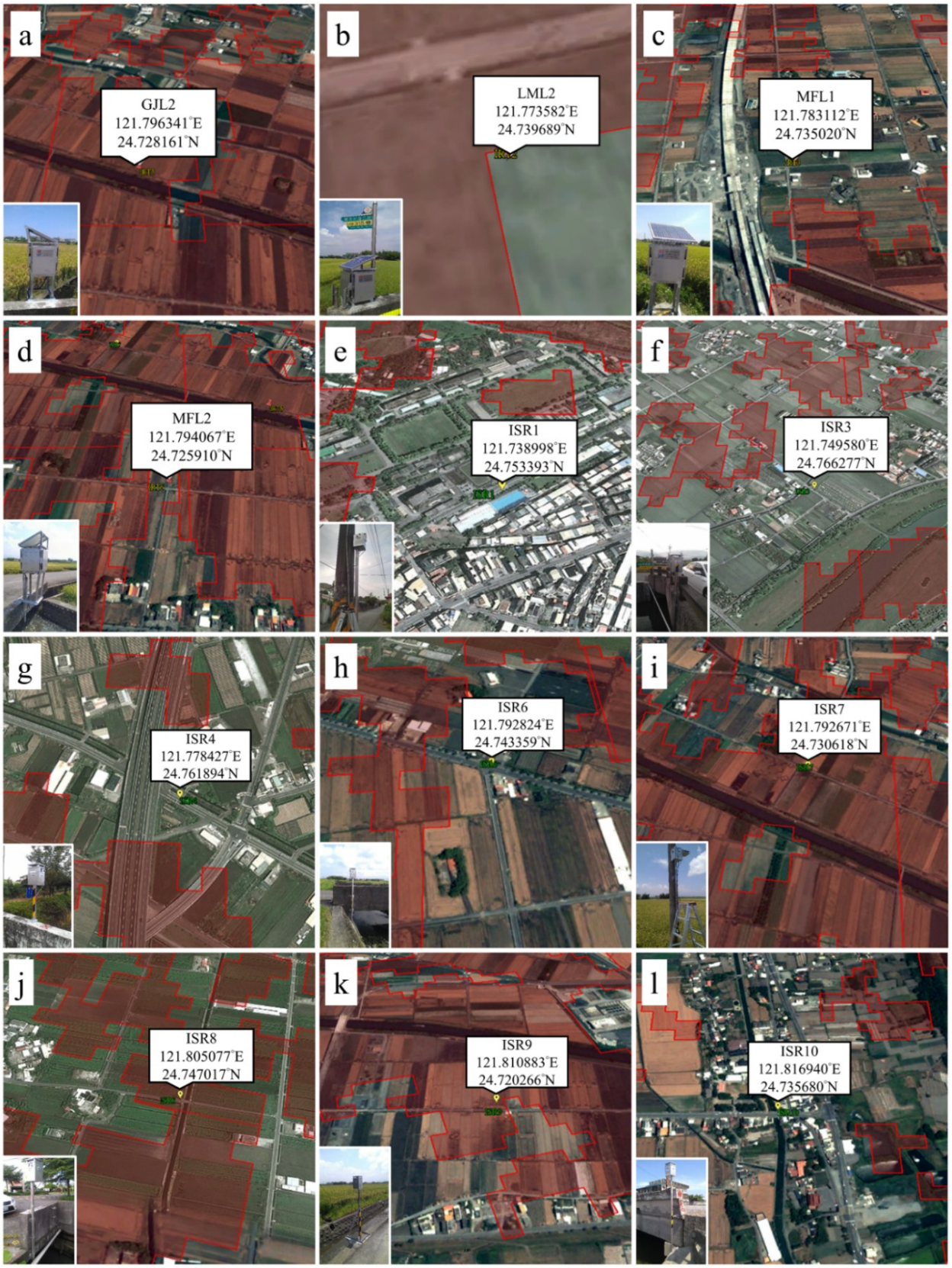

Figure 9. The close-up photo of the water level gauge and the inundated areas (red shaded polygons) interpreted from the SAR imagery of twelve stations: (**a**) GJL12, (**b**) LML2, (**c**) MFL1, (**d**)MFL2, (**e**) ISR1, (**f**) ISR3, (**g**) ISR4, (**h**) ISR6, (**i**) ISR7, (**j**) ISR8, (**k**) ISR9, (**l**) ISR10, the name and location of each station is defined and illustrated in Figure 3 that were fully in accordance with the interpretation results.

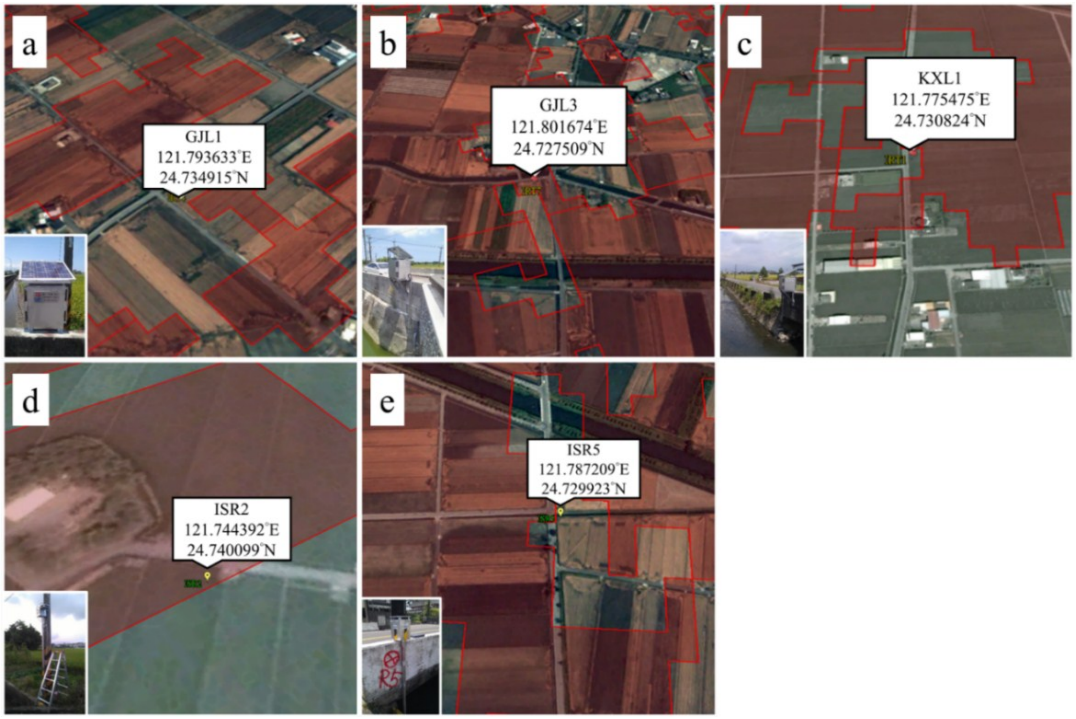

Figure 10. The close-up photo of water level gauge and the inundated areas (red shaded polygons) interpreted from the SAR imagery of five stations: (**a**) GJL1, (**b**) GJL3, (**c**) KXL1, (**d**)ISR2, (**e**) ISR5, the name and location of each station is defined and illustrated in Figure 3 that were not consist with the interpretation results. These five stations are all located in a mixed pixel near the boundary of the inundated area.

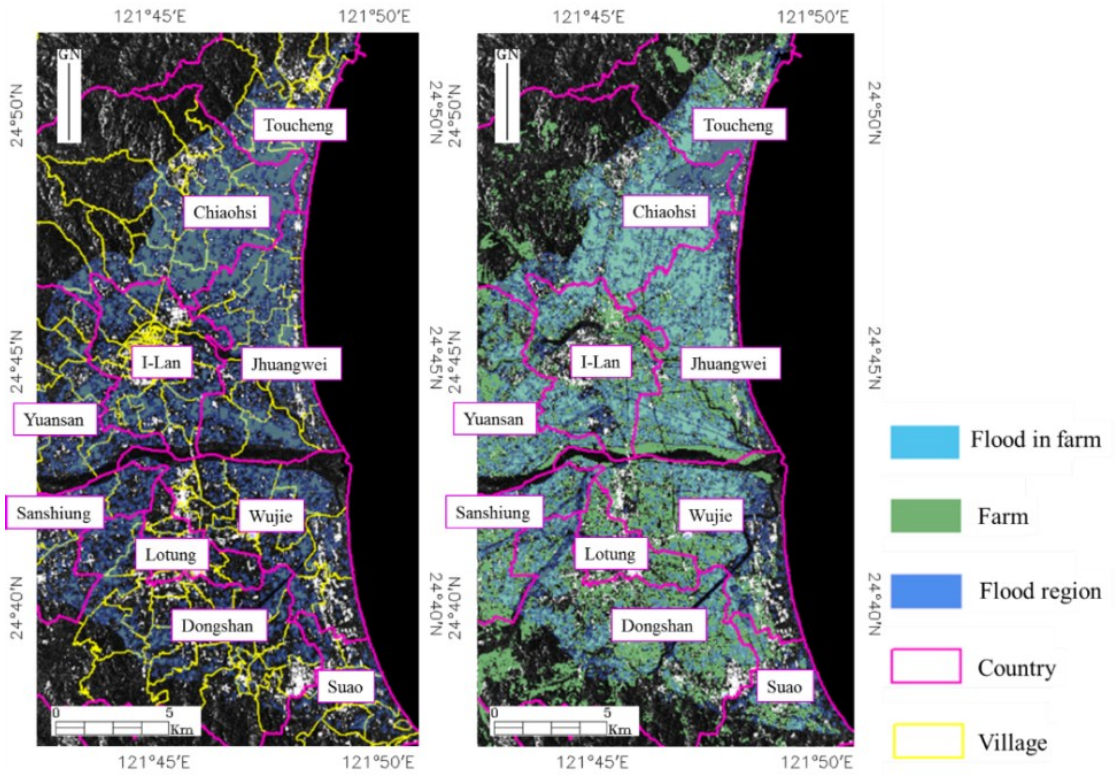

Figure 11. The flooded regions in I-Lan County, with a focus on farmland areas.

By combining the data for the flooded regions, village administrative maps and land use maps, the damage to villages and farmland can be assessed. The results, as shown in Figure 11, can be used as references for disaster damage assessment. The government can thus allocated some of its agricultural budget to help farmers based on this flood map.

5.2. Inundation Depth

This research compared the flooded regions that were derived from the SAR image with the inundation potential maps produced by the WRA from 2007 to 2010, and the relationship between these can be used to estimate the water depths at the time the image was taken. The method used to retrieve the flood depth is collecting hourly data of precipitation and related hydraulic information and entering these data into the inundation model. The model can then derive the flood potential map with both the flood depth and region for each hour of the specific event. When combined with the flood regions that are calculated from the near real-time radar satellite image, the model can start deriving the flood depths. The best fit for the inundation potential data with 200 mm rainfall in one day is marked in Table 2. Table 2 shows the accuracy between the flood extent map and different inundation potential maps. I is the different time intervals of the recurrence period; I1–I500 are 1–500 years; R is the different intensities of rainfall; R200–R600 are 200 mm–600 mm in one day.

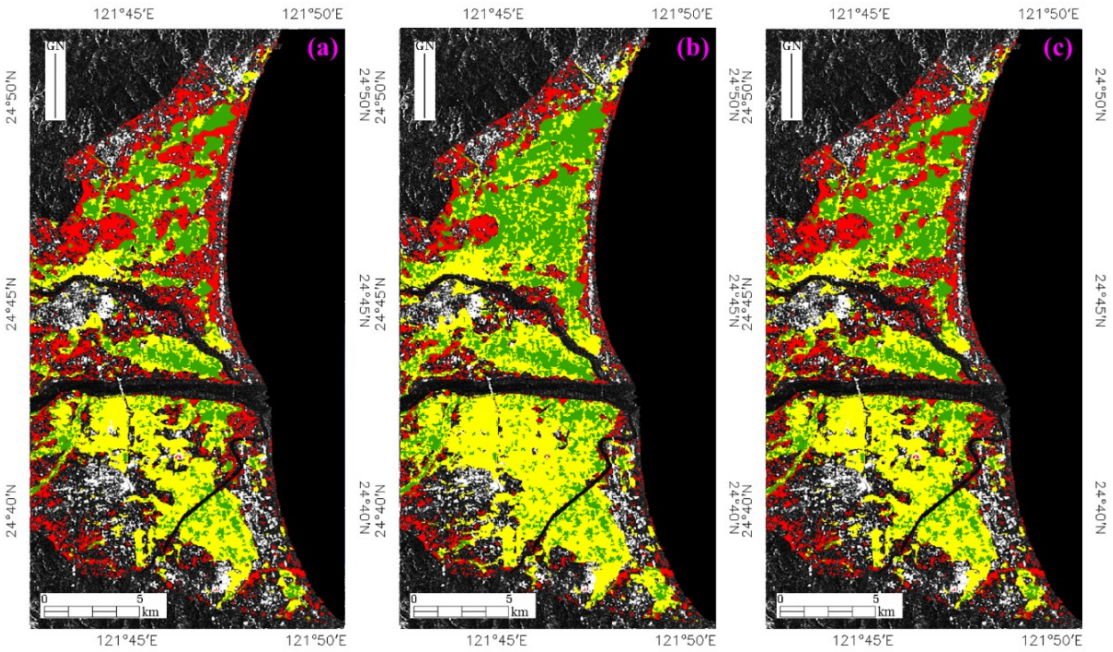

Figure 12. The flood extent map compared to different inundation potential maps. Yellow regions show the common areas between the flood extent map and the inundation potential map; green regions show the areas overestimated by the inundation potential map; and red regions show the areas underestimated by the inundation potential map. (**a**) Comparison of the flood extent map to 200 mm rainfall map in one day. (**b**) Comparison of the flood extent map to the one-year recurrence period inundation potential map. (**c**) Comparison of the flood extent map to the two-year recurrence period inundation potential map.

Figure 12 shows the flood extent map compared to different inundation potential maps on 13 July 2013 during Typhoon Soulik. The yellow regions show the common areas between the flood extent map and inundation potential map, while green regions show the areas overestimated by the inundation potential map, and the red regions show the areas underestimated by the inundation potential map. Figure 12a compares the results of the flood extent map to 200 mm rainfall in one day. Figure 12b shows the results of the flood extent map compared to the one-year recurrence period inundation potential map. Figure 12c shows the results of the flood extent map compared to the two-year recurrence period inundation potential map. In these images, Figure 12a shows the highest fit with regard to the inundation potential, with the flood depth map produced using Figure 12a shown in Figure 13.

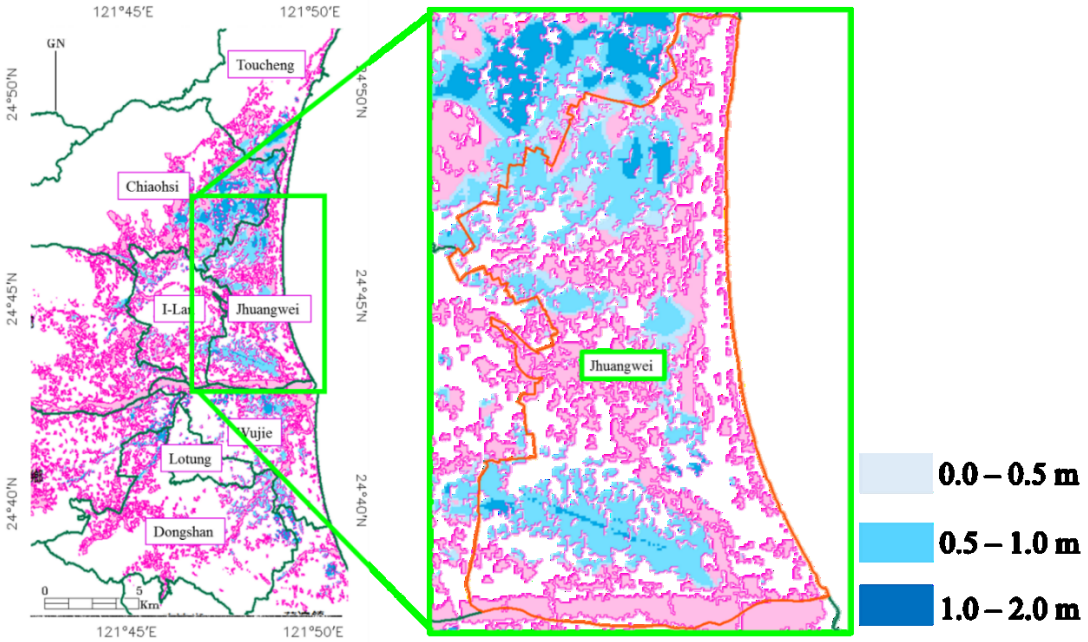

Figure 13. The flood depth map derived in this research.

Field observation data from water level stations were used to validate the results of the flood depth map, with the results shown in Table 3. Most of the points in the flood depth map were overestimated, and only two stations (GJL2 and ISR8) were underestimated. Note that the inundation potential maps were generated from 2007 to 2010 using all historical data. Many drainage systems had already been improved before Typhoon Soulik. As a result, the actual depths of flood are lower than our estimation in most of the regions. In any case, those two regions with underestimated flood depths suggest that the authorities examine the status of the related drainage systems.

Table 2. The accuracy between the flood extent map and different inundation potential maps.

	Area of Inundation Potential Map (m^2)	Area of Flood Extent Map (m^2)	Fit Area (m^2)	Overestimated Area of Inundation Potential Map (m^2)	Overestimated Area of Flood Extent Map (m^2)	Consistent Rate	Overestimation Rate of Flood Extent Map	Underestimation Rate of Flood Extent Map	Accuracy
Symbol	A	B	C	A – C = D	B – C = E	C/B = F	D/B = G	E/B = H	F/G = I
I1	80,203,200	84,444,893	32,336,135	47,867,065	52,108,758	0.3829	0.5668	0.6171	0.68
I10	135,708,800	84,444,893	52,866,069	82,842,732	31,578,825	0.626	0.981	0.374	0.64
I100	156,982,400	84,444,893	59,381,731	97,600,669	25,063,163	0.7032	1.1558	0.2968	0.61
I2	110,441,600	84,444,893	44,185,098	66,256,502	40,259,795	0.5232	0.7846	0.4768	0.67
I20	143,035,200	84,444,893	55,200,726	87,834,474	29,244,167	0.6537	1.0401	0.3463	0.63
I200	161,609,600	84,444,893	60,716,539	100,893,061	23,728,354	0.719	1.1948	0.281	0.60
I25	145,214,400	84,444,893	55,817,560	89,396,840	28,627,333	0.661	1.0586	0.339	0.62
I5	126,550,400	84,444,893	49,885,001	76,665,399	34,559,892	0.5907	0.9079	0.4093	0.65
I50	151,299,200	84,444,893	57,693,123	93,606,077	26,751,771	0.6832	1.1085	0.3168	0.62
I500	167,080,000	84,444,893	62,111,361	104,968,639	22,333,532	0.7355	1.243	0.2645	0.59
R200	93,379,200	84,444,893	38,036,356	55,342,844	46,408,537	0.4504	0.6554	0.5496	0.69
R350	120,953,600	84,444,893	48,213,636	72,739,964	36,231,258	0.5709	0.8614	0.4291	0.66
R450	133,155,200	84,444,893	52,209,337	80,945,863	32,235,556	0.6183	0.9586	0.3817	0.64
R600	147,368,000	84,444,893	56,693,289	90,674,711	27,751,605	0.6714	1.0738	0.3286	0.63

Table 3. Comparison between the flood extent map and different inundation potential maps.

Name	Derived Flood Depth (cm)	Water Level Station (cm)	Flood	Annotations
GJL1	61.9	30.7	○	Flood depth overestimated.
GJL2	66.0	93.9	○	The water level station is located at the edge of a water body.
GJL3	62.5	0.1	○	Flood depth underestimated.
KXL1	70.9	48.1	×	Flood depth overestimated.
LML2	0.0	1.7	×	The water level station is located at the edge of a water body.
MFL1	69.6	1.6	×	Flood depth overestimated.
MFL2	64	0.8	×	The water level station is located at the edge a water body.
ISR1	0.0	0.4	×	The results are consistent with the water level station data.
ISR2	37.7	0.3	○	Flood depth overestimated.
ISR3	113.5	0.6	×	Flood depth overestimated.
ISR4	0.0	0.4	×	The results are consistent with the water level station data.
ISR5	66.5	21.2	×	Flood depth overestimated.
ISR6	0.0	0.3	×	The water level station is located at the edge a water body.
ISR7	62.8	10.2	○	Flood depth overestimated.
ISR8	0.0	30.3	○	The results are consistent with water level station data.
ISR9	36.6	5.4	○	Flood depth overestimated.
ISR10	38.4	0.5	×	The water level station is located at the edge a water body.

6. Concluding Remarks

Floods are one of the most frequently-occurring natural disasters, which cause damage, human suffering and economic losses [35]. Thus, it is important to develop more effective approaches to flood monitoring. There are two important issues in such monitoring: flood extent and flood depth. However, optical satellite images cannot monitor floods through cloud or fog, and thus, many researchers have worked to detect floods based on SAR imagery.

This research reports the successful case of a rapid response to a flash flood in I-Lan County in Taiwan, using a map of inundated areas derived from COSMO-SkyMed imagery within 24 hours. The flood was caused by the intensive precipitation brought by Typhoon Soulik in July 2013. Based on the ensemble forecasts of the trajectory provided by the CWB, an urgent request for spaceborne SAR imagery was made 24 hours before Typhoon Soulik made landfall. Two COSMO-SkyMed images were successfully acquired when the center of Typhoon Soulik had just crossed the northern part of Taiwan. The SAR-derived map of the inundated areas was published on a web-based platform powered by Google Earth within 24 hours, with the aim of supporting the decision-making processes related to disaster prevention and mitigation.

A detailed validation was made by comparing the map with *in situ* data of the water levels at 17 stations, as collected by TTFRI. This data were used to validate the flood extent map. There were five water level stations that were located at the edge of water bodies. The remaining 12 stations were fully in accordance with the interpretation results. The approach we proposed to infer the flood depth is based on the comparison between the flood extent map and different inundation potential maps. It is basically an indirect approach, and its accuracy is limited by the quality of the inundation potential maps. The improvement of the drainage system would mitigate the level of inundation, as well.

The results demonstrate the feasibility of rapidly responding to a typhoon-induced flood with a spaceborne SAR-derived map of inundated areas. A standard operating procedure was derived from this work, and this was then adopted by the WHMC of the WRA, Taiwan, in subsequent typhoon seasons, such as Typhoon Trami (August 2013) and Typhoon Soudelor (August 2015). Together with the number and distribution of existing engine-driven pumps, WHMC is able to calculate the pumping capacity at all flood hotspots and to make the best use of all engine-driven pumps available. The derived map of flood depth also serves as an important reference to claim for compensation in the aftermath of the flood event.

Acknowledgments

This research is supported by the Ministry of Science and Technology of the Republic of China, (Taiwan), under Contract Nos. MoST 103-2611-M-006-001 and MoST 103-2627-B-006-006. The authors acknowledge support from Taiwan Typhoon and Flood Research Institute, National Applied Research Laboratories, in providing the Taiwan Cooperative Precipitation Ensemble Forecast Experiment results.

Author Contributions

Hsiao-Wei Chung organized the research and drafted the manuscript. Cheng-Chien Liu designed and proposed the main structure of this research. I-Fan Cheng and Yun-Ruei Lee processed the data that were used in this research. Ming-Chang Shieh provided the remote sensing data and field observation data, as well as the research topic. All authors contributed useful suggestions and comments in the process of preparing this manuscript.

Conflicts of Interest

The authors declare no conflicts of interest.

References

1. Skakun, S.; Kussul, N.; Shelestov, A.; Kussul, O. Flood hazard and flood risk assessment using a time series of satellite images: A case study in Namibia. *Risk Anal.* **2014**, *34*, 1521–1537.
2. Greifeneder, F.; Wagner, W.; Sabel, D.; Naeimi, V. Suitability of sar imagery for automatic flood mapping in the lower Mekong Basin. *Int. J. Remote Sens.* **2014**, *35*, 2857–2874.
3. Liu, C.C.; Liu, J.G.; Lin, C.W.; Wu, A.M.; Liu, S.H.; Shieh, C.L. Image processing of Formosat-2 data for monitoring the south Asia tsunami. *Int. J. Remote Sens.* **2007**, *28*, 3093–3111.
4. Liu, C.-C.; Chen, N.-Y. Responding to natural disasters with satellite imagery. *SPIE Newsroom* **2011**, doi:10.1117/2.1201106.003758.
5. Schumann, G.; Bates, P.D.; Horritt, M.S.; Matgen, P.; Pappenberger, F. Progress in integration of remote sensing-derived flood extent and stage data and hydraulic models. *Rev. Geophys.* **2009**, *47*, RG4001.
6. Rango, A.; Salomons, V.V. Regional flood mapping from space. *Water Resour. Res.* **1974**, *10*, 473–484.
7. Wang, Q.; Watanabe, M.; Hayashi, S.; Murakami, S. Using noaa avhrr data to assess flood damage in China. *Environ. Monit. Assess.* **2003**, *82*, 119–148.

8. Zhang, F.; Zhu, X.; Liu, D. Blending modis and landsat images for urban flood mapping. *Int. J. Remote Sens.* **2014**, *35*, 3237–3253.
9. Feng, Q.; Liu, J.; Gong, J. Urban flood mapping based on unmanned aerial vehicle remote sensing and random forest classifier—A case of Yuyao, China. *Water* **2015**, *7*, 1437–1455.
10. Jung, Y.; Kim, D.; Kim, D.; Kim, M.; Lee, S.O. Simplified flood inundation mapping based on flood elevation-discharge rating curves using satellite images in gauged watersheds. *Water* **2014**, *6*, 1280–1299.
11. Chaouch, N.; Temimi, M.; Hagen, S.; Weishampel, J.; Medeiros, S.; Khanbilvardi, R. A synergetic use of satellite imagery from sar and optical sensors to improve coastal flood mapping in the Gulf of Mexico. *Hydrol. Process.* **2012**, *26*, 1617–1628.
12. Pulvirenti, L.; Pierdicca, N.; Boni, G.; Fiorini, M.; Rudari, R. Flood damage assessment through multitemporal COSMO-SkyMed data and hydrodynamic models: The Albania 2010 case study. *IEEE J. Sel. Top. Appl. Earth Obs. Remote Sens.* **2014**, *7*, 2848–2855.
13. Yulianto, F.; Sofan, P.; Zubaidah, A.; Sukowati, K.A.D.; Pasaribu, J.M.; Khomarudin, M.R. Detecting areas affected by flood using multi-temporal alos PALSAR remotely sensed data in Karawang, West Java, Indonesia. *Nat. Hazards* **2015**, *77*, 959–985.
14. Goroshko, M.V.; Gil'manova, G.Z.; Rybas, O.V. Analysis of digital elevation models of the geological surveys of the Elkon Uranium-Ore District (Aldan-Stanovoi Shield). *Russ. J. Pac. Geol.* **2015**, *9*, 136–140.
15. Skrunes, S.; Brekke, C.; Eltoft, T.; Kudryavtsev, V. Comparing near-coincident C- and X-band SAR acquisitions of marine oil spills. *IEEE Trans. Geosci. Remote Sens.* **2015**, *53*, 1958–1975.
16. Vicente-Guijalba, F.; Martinez-Marin, T.; Lopez-Sanchez, J.M. Dynamical approach for real-time monitoring of agricultural crops. *IEEE Trans. Geosci. Remote Sens.* **2015**, *53*, 3278–3293.
17. Zhang, L.; Guo, H.; Li, X.; Wang, L. Ecosystem assessment in the Tonle Sap Lake region of Cambodia using Radarsat-2 wide fine-mode Sar data. *Int. J. Remote Sens.* **2014**, *35*, 2875–2892.
18. Horritt, M.S.; Mason, D.C.; Luckman, A.J. Flood boundary delineation from synthetic aperture radar imagery using a statistical active contour model. *Int. J. Remote Sens.* **2001**, *22*, 2489–2507.
19. Imhoff, M.L.; Vermillion, C.; Story, M.H.; Choudhury, A.M.; Gafoor, A.; Polcyn, F. Monsoon flood boundary delineation and damage assessment using space borne imaging radar and Landsat data. *Photogramm. Eng. Remote Sens.* **1987**, *53*, 405–413.
20. Mason, D.C.; Davenport, I.J.; Neal, J.C.; Schumann, G.J.P.; Bates, P.D. Near real-time flood detection in urban and rural areas using high-resolution synthetic aperture radar images. *IEEE Trans. Geosci. Remote Sens.* **2012**, *50*, 3041–3052.
21. Kundu, S.; Aggarwal, S.P.; Kingma, N.; Mondal, A.; Khare, D. Flood monitoring using microwave remote sensing in a part of Nuna River Basin, Odisha, India. *Nat. Hazards* **2015**, *76*, 123–138.
22. Manjusree, P.; Kumar, L.P.; Bhatt, C.M.; Rao, G.S.; Bhanumurthy, V. Optimization of threshold ranges for rapid flood inundation mapping by evaluating backscatter profiles of high incidence angle Sar images. *Int. J. Disaster Risk Sci.* **2012**, *3*, 113–122.
23. Voigt, S.; Kemper, T.; Riedlinger, T.; Kiefl, R.; Scholte, K.; Mehl, H. Satellite image analysis for disaster and crisis-management support. *IEEE Trans. Geosci. Remote Sens.* **2007**, *45*, 1520–1528.

24. Giustarini, L.; Vernieuwe, H.; Verwaeren, J.; Chini, M.; Hostache, R.; Matgen, P.; Verhoest, N.E.C.; De Baets, B. Accounting for image uncertainty in SAR-based flood mapping. *Int. J. Appl. Earth Obs. Geoinform.* **2015**, *34*, 70–77.
25. CDPRC. Central disaster prevention and response council. Available online: http://www.Cdprc.Ey.Gov.Tw/default.Aspx (accessed on 13 July 2013).
26. CWB. Central weather bureau, typhoon database. Available online: http://rdc28.Cwb.Gov.Tw/tdb/ntdb/pagecontrol/ty_warning (accessed on 13 July 2013).
27. Lillesand, T.; Kiefer, R.W.; Chipman, J. *Remote Sensing and Image Interpretation*, 7th ed.; John Wiley & Sons, Inc.: Hoboken, NJ, USA, 2015; p. 768.
28. Refice, A.; Capolongo, D.; Pasquariello, G.; D'Addabbo, A.; Bovenga, F.; Nutricato, R.; Lovergine, F.P.; Pietranera, L. SAR and InSAR for flood monitoring: Examples with COSMO-SkyMed data. *IEEE J. Sel. Top. Appl. Earth Obs. Remote Sens.* **2014**, *7*, 2711–2722.
29. Liu, C.-C. Preparing a landslide and shadow inventory map from high-spatial-resolution imagery facilitated by an expert system. *J. Appl. Remote Sens* **2015**, *9*, 096080-1–096080-13.
30. Martinis, S.; Twele, A.; Voigt, S. Unsupervised extraction of flood-induced backscatter changes in SAR data using Markov image modeling on irregular graphs. *IEEE Trans. Geosci. Remote Sens.* **2011**, *49*, 251–263.
31. Wu, S.-J.; Hsu, C.-T.; Lien, H.-C.; Chang, C.-H. Modeling the effect of uncertainties in rainfall characteristics on flash flood warning based on rainfall thresholds. *Nat. Hazards* **2015**, *75*, 1677–1711.
32. Mtamba, J.; van der Velde, R.; Ndomba, P.; Zoltan, V.; Mtalo, F. Use of Radarsat-2 and Landsat TM images for spatial parameterization of manning's roughness coefficient in hydraulic modeling. *Remote Sens.* **2015**, *7*, 836–864.
33. Proud, S.R.; Fensholt, R.; Rasmussen, L.V.; Sandholt, I. Rapid response flood detection using the MSG geostationary satellite. *Int. J. Appl. Earth Obs. Geoinform.* **2011**, *13*, 536–544.
34. Amarnath, G. An algorithm for rapid flood inundation mapping from optical data using a reflectance differencing technique. *J. Flood Risk Manag.* **2014**, *7*, 239-250.
35. Li, L.; Chen, Y.; Yu, X.; Liu, R.; Huang, C. Sub-pixel flood inundation mapping from multispectral remotely sensed images based on discrete particle swarm optimization. *Isprs J. Photogramm. Remote Sens.* **2015**, *101*, 10–21.